

To be published in *The Astrophysical Journal*, Vol. **492**, Jan 10th, 1998

# The physics of twisted magnetic tubes rising in a stratified medium: two dimensional results

Emonet, T., Moreno-Insertis, F.

*Instituto de Astrofísica de Canarias, 38200 La Laguna (Tenerife), Spain*

*temonet@ll.iac.es, fmi@ll.iac.es*

## ABSTRACT

The physics of a twisted magnetic flux tube rising in a stratified medium is studied using a numerical MHD code. The problem considered is fully compressible (no Boussinesq approximation), includes ohmic resistivity, and is two dimensional, i.e., there is no variation of the variables in the direction of the tube axis. We study a high plasma  $\beta$  case with small ratio of radius to external pressure scaleheight. The results obtained can therefore be of relevance to understand the transport of magnetic flux across the solar convection zone.

We confirm that a sufficient twist of the field lines around the tube axis can suppress the conversion of the tube into two vortex rolls. For a tube with relative density deficit of order  $1/\beta$  (the classical Parker buoyancy) and radius smaller than a pressure scaleheight ( $R^2 \ll H_p^2$ ), the minimum amount of twist necessary corresponds to an average pitch angle of order  $\sin^{-1}[(R/H_p)^{1/2}]$ . The evolution of a tube with this degree of twist is studied in detail, including the initial transient phase, the internal torsional oscillations and the asymptotic, quasi-stationary phase. During the initial phase, the outermost, weakly magnetized layers of the tube are torn off its main body and endowed with vorticity. They yield a trailing magnetized wake with two vortex rolls. Which fraction of the total magnetic flux is brought to the wake is a function of the initial degree of twist. In the weakly twisted case, most of the initial tube is turned into vortex rolls. At the opposite end (strong initial twist), the tube rises with only a small deformation and no substantial loss of magnetic flux. The formation of the wake and the loss of flux from the main body of the tube are basically complete after the initial transient phase.

A sharp interface between the tube interior and the external flows is formed at the tube front and sides; it has the characteristic features of a magnetic boundary layer. Its structure is determined as an equilibrium between ohmic diffusion and field advection through the external flows. It is the site of vorticity generation via the magnetic field during the whole tube evolution.

From the hydrodynamical point of view, this problem constitutes an intermediate case between the rise of air bubbles in water and the motion of a rigid cylinder in an external medium. As in the first one, the tube is deformable and the outcome of the experiment (shape of rising object and wake) depends on the value of the Weber number. Several structural features obtained in the present simulation are also observed in rising air bubbles, like a central *tail*, and a *skirt* enveloping the wake. As in rigid cylinders, the boundary layer satisfies a no-slip condition (provided for in the tube by the magnetic field), and secondary rolls are formed at the lateral edges of the moving object.

*Subject headings:* Magnetohydrodynamics: MHD, Hydrodynamics, Sun: Magnetic Fields, Magnetic Fields, Sun: Activity, Stars: Magnetic Fields

## 1. Introduction

The rise of magnetic flux from the deep levels of the solar convection zone to the photosphere is a complex phenomenon involving many different magnetic and hydrodynamical processes. Particular attention has been devoted in the past 20 years to the time-evolution of a single buoyant magnetic flux tube considered as a one-dimensional object (Moreno-Insertis 1986; Choudhuri 1989; D'Silva & Choudhuri 1993; Fan, Fisher & DeLuca 1993; Fan, Fisher & McClymont 1994; Caligari et al. 1995). Further references and a recent review can be found in the paper by Moreno-Insertis 1997a). These calculations incorporate several aspects of the basic physics of the rise of the magnetic tubes (buoyancy, magnetic and rotational forces, external stratification, etc). They have been successful in predicting morphological and kinematic features of the resulting active regions which are observed at the surface of the Sun.

Yet, the assumption of one-dimensionality of the magnetic region is certainly a drastic simplification. From laboratory and numerical experiments in different contexts we know of the complicated hydrodynamical and magnetic structure within and outside a tubular object which is moving with respect to the surrounding fluid. The one-dimensional numerical models mentioned above, in particular, do not contain two ingredients which turn out to be fundamental in studying the rise of buoyant magnetized plasma regions, to wit, the vorticity of the velocity field and the twist of the field lines around the main axis of the tube.

Vorticity and transverse field components may be crucial for the formation of the tubes in the first place (Cattaneo & Hughes 1988; Cattaneo, Chiueh, & Hughes 1990; Matthews, Hughes & Proctor 1995). They also play a central role in the time evolution of the rising magnetic region. A clear warning in this sense came from the work of Schüssler (1979), who showed how the cross section of a straight, buoyant magnetic tube initially with the same temperature of its surroundings develops an *umbrella* shape (two side lobes connected on their upper side by an arch). The side lobes rotate in opposite directions around a horizontal axis, each thus constituting a vortex tube; they finally detach from each other and from the arch above them. The whole process occurs at the beginning of the rise, namely before the tube has risen across a height equivalent to a few times its

own diameter. The physics involved has been considered in detail by Longcope, Fisher & Arendt (1996). These authors have studied the Boussinesq problem, including untwisted and very weakly twisted magnetic tubes. They clearly show how the two rotating side lobes, when detached from the rest, are subjected to a downward-pointing lift force, as a result of their flow being non-circulation free. The lift ends up cancelling the buoyancy force, this being the reason for their horizontal asymptotic motion. If this were a universal mechanism operating on all rising magnetic flux tubes, then magnetic buoyancy should no longer be considered an efficient mechanism to bring magnetic flux to the photosphere.

In the present paper we consider in detail the more general case of a buoyant magnetic flux tube with an arbitrary initial twist of the field lines (but still horizontal and with uniform values of all variables along the direction of the axis). The transverse magnetic field (i.e., the component of the field vector normal to the tube axis) imparts a certain rigidity to the tube cross section. If strong enough, it can prevent the conversion of the tube into a vortex tube pair. The minimum amount of twist necessary for that corresponds to an average pitch angle of order  $\sin^{-1}\{[R/H_p \beta/2 |\Delta\rho/\rho|]^{1/2}\}$ , with  $R$  the tube radius,  $H_p$  the external pressure scaleheight, and  $\Delta\rho$  the density difference between tube and surroundings (see §3.1). This approximate criterion is indeed fulfilled by magnetic tubes with the classical Parker magnetic buoyancy, as shown in a preliminary presentation of this paper (Moreno-Insertis & Emonet 1996). In the present article, we explore in more detail the physics involved in that process, discussing a number of (M)HD processes occurring inside the tube, in the boundary layer at its periphery and in the trailing wake. We also show how the results of Schüssler (1979) and Longcope et al.(1996) can be seen as the limiting case in which the trailing wake in fact engulfs most of the original rising tube. The pitch angle just mentioned thus signals the borderline between the weak and strong twist regimes: a buoyant tube with an initial twist above that level rises without being strongly deformed and is followed by a wake containing only a small fraction of the initial total magnetic flux.

Additionally to the work of Moreno-Insertis & Emonet (1996), there is another paper in the recent literature dealing with a related subject (Cargill et al. 1996). The authors have studied the interaction

of a twisted tube with a magnetized medium in the absence of gravity when the tube is subjected to an ad-hoc, spatially uniform acceleration. Special emphasis was put on the reconnection of the ambient magnetic field with the tube's own one. Buoyancy, stratification, or different degrees of twist were not studied in that paper. Two further papers, submitted simultaneously with the present one, deal with the rise of buoyant twisted magnetic tubes (Fan, Zweibel & Lantz 1997; Hughes, Falle & Joarder, 1998). The first authors, in particular, study the interaction between tubes rising in pairs. The results of both papers concerning the rise of single tubes are in general agreement with those of Moreno-Insertis & Emonet (1996).

The layout of the paper is as follows. After a brief presentation of the equations and the numerical procedure in §2, the basic features of the physical problem are considered (§3). This includes the main parameters and a discussion of the amount of twist necessary to prevent the deformation of the tube and its conversion into vortex rolls. In §4, the simulation of the rise of a tube with that amount of twist is presented. In particular, the initial acceleration phase, the internal torsional oscillations and the later asymptotic phase are discussed. Section §5 deals with the structure of the magnetic boundary layer around the tube, and §6 examines the trailing wake. Finally, the transition between the twisted and untwisted case is explained in §7. A general discussion follows in §8.

## 2. Equations and numerical procedure

### 2.1. Equations

Our medium is an ideal compressible and stratified gas governed by the general equations of the magnetohydrodynamics (MHD) including Ohmic diffusion:

$$\frac{D\rho}{Dt} = -\rho\nabla \cdot \mathbf{v}, \quad (1)$$

$$\rho\frac{D\mathbf{v}}{Dt} = -\nabla p + \frac{1}{4\pi}(\nabla \times \mathbf{B}) \times \mathbf{B} + \rho\mathbf{g}, \quad (2)$$

$$\frac{\partial \mathbf{B}}{\partial t} = \nabla \times (\mathbf{v} \times \mathbf{B}) + \eta\Delta\mathbf{B}, \quad (3)$$

$$\rho\frac{De}{Dt} = -p\nabla \cdot \mathbf{v} + \frac{\eta}{4\pi}(\nabla \times \mathbf{B})^2, \quad (4)$$

with  $e$  the internal energy per unit mass and  $\eta$  the ohmic diffusivity, which is assumed constant. All

other symbols have their customary meaning. Cartesian coordinates  $(x, y, z)$  are adopted so that the  $z$ -direction is anti-parallel to  $\mathbf{g}$ . In this paper we consider a two-dimensional problem: we assume that there are no variations of the physical variables along the  $y$ -axis ( $\partial/\partial y \equiv 0$ ), although  $B_y$  and  $v_y$  are generally non zero.

Equations (1)–(4) are cast in their conservative form and solved with a code written by Shibata 1983. The latter is based on a modified Lax-Wendroff scheme (Rubin & Burstein 1967) and stabilized with artificial viscosity as described by Richtmyer & Morton (1967). The inclusion of physical resistivity in our equations and the absence of any shock phenomena in the solutions permit us to minimize the use of the artificial viscosity. The latter is restricted, in any case, to regions of very steep gradients only.

This code has been repeatedly tested and used for two-dimensional simulations of the outbreak of the magnetic field at the surface of the Sun by Shibata and collaborators (see e.g. Shibata 1983; Shibata et al. 1989; Kaisig et al. 1990). In addition, we have successfully run several tests for our problem, checking for the convergence of the code as well as for the conservation of mass, energy and magnetic flux in the box.

In this paper, we only consider a case with left-right symmetry about a vertical plane containing the tube axis. For each half of the tube we use a numerical grid of 300 points in the horizontal direction and 700 points in the vertical one (although in the figures presented here, only a small fraction of the box is shown). In the following, the results are given in dimensionless form, using as units the background density, pressure scaleheight and Alfvén speed calculated at the center of the tube at time  $t = 0$ .

### 2.2. Initial conditions

The initial condition consists of an unperturbed background atmosphere, with pressure  $p_e$  and density  $\rho_e$ , and, superimposed, a perturbation associated with a magnetic flux tube. To avoid any confusion due to pseudo-convective effects, the background atmosphere is adiabatically stratified. It spans vertically 80% of the pressure scaleheight at the bottom of the box. The pressure contrast between the top and bottom is 2.6. The density contrast is 1.8.

After inclusion of the magnetic tube, the resulting system satisfies the following simple condition:

$-\nabla \Delta p + \mathbf{J}/c \times \mathbf{B} = 0$ , with  $\Delta p \stackrel{\text{def}}{=} p - p_e$  the pressure excess as compared with the background stratification,  $\mathbf{J}$  the electric current density and  $c$  the speed of light. In the absence of gravity, this would be a perfect equilibrium condition. The density profile in the magnetic region is determined by assuming that the entropy in the tube is constant and equal to the unperturbed value in the atmosphere. The tube at time  $t = 0$  is thus buoyant ( $\rho < \rho_e$ ) and fulfills

$$\frac{\Delta \rho}{\rho} \stackrel{\text{def}}{=} \frac{\rho - \rho_e}{\rho} \simeq -\frac{1}{\gamma \beta} \quad (5)$$

to first order in  $1/\beta$ , with  $\gamma$  the specific heat ratio. This case is intermediate between the two extreme possibilities of full thermal equilibrium, i.e.,  $T = T_e$  (which would be a factor  $\gamma$  more buoyant) and the case of a tube with  $\rho = \rho_e$ . The evolution presented here is qualitatively very similar to the first case, whereas it deviates in important respects from the second.

Along this paper we will deal with a number of different magnetic field profiles at time  $t = 0$ . The longitudinal field  $B_l = B_y$  will be taken to have a gaussian profile,

$$B_l(t = 0) \propto \exp(-r^2/R^2). \quad (6)$$

The transverse field  $B_t(t = 0)$  is chosen to be purely azimuthal; calling  $r$  and  $\phi$  the polar coordinates around the tube center, we have  $\mathbf{B}_t(t = 0) = B_\phi \mathbf{e}_\phi$ . For  $B_\phi$ , we will choose distributions such that the pitch angle  $\Psi$ ,

$$\Psi \stackrel{\text{def}}{=} \tan\left(\frac{B_\phi}{B_l}\right), \quad (7)$$

adopts an asymptotically flat profile:

$$B_\phi \propto B_l \frac{ar^n}{ar^n + R^n}, \quad (8)$$

or, alternatively, an exponentially decaying one:

$$B_\phi \propto B_l \left(\frac{1}{\sqrt{n}} \frac{r}{R}\right)^n \exp\left(-\frac{r^2}{R^2} + \frac{n}{2}\right), \quad (9)$$

The choice of  $n$  determines the *rigidity* of the tube center. In this paper we consider the case  $n = 3$  and  $a = 0.9$ . As we will see, both profiles (8) and (9) yield basically the same time evolution (§5.1). As explained in the discussion, we have also run some tests with flat, top-hat magnetic profiles (§8.1).

## 2.3. Boundary conditions

The side and bottom boundaries are closed lids. A closed boundary at the top of the box must be avoided for two reasons: (1) the sound waves generated by the tube in the external medium must be able to leave the box and (2) the rise of the tube should not be unduly braked through the excess pressure at a closed boundary at the top. An ideal *free* boundary should be transparent for the outgoing disturbances and should not introduce disturbances through incoming waves. In the present calculations we achieve this by introducing a *fiducial layer* (Nordlund & Stein 1990) well above the upper boundary of the box. At each time step, the pressure in the fiducial layer is calculated by assuming that each point in it is in static equilibrium with respect to the point on the boundary of the box lying directly below it; the densities are then obtained via the constant background entropy; the velocity is set to zero in the fiducial layer. The net mass flux across the boundary is not necessarily zero. However, the total mass of the box only varies by a maximum factor of  $10^{-6}$  during each single run.

## 3. The physical problem: parameters governing the evolution

The present physical problem is characterized by four basic dimensionless input parameters: (1) the thickness of the tube in units of the local pressure scale height,  $\tilde{R} \stackrel{\text{def}}{=} R/H_p$ ; (2) the plasma beta at the center of the tube,  $\beta_0$ ; (3) the ratio between the transverse and the longitudinal component of the field, as measured by, e.g., the pitch angle at a representative position of the tube,  $\Psi_{mt}$ , to be specified in the following; (4) the ohmic diffusivity  $\eta$  in terms of, e.g.,  $v_A H_p$ , with  $v_A$  the Alfvén speed:  $\tilde{\eta} \stackrel{\text{def}}{=} \eta/(v_A H_p)$ .

These parameters determine the properties of the initial magnetic tube and are independent of the velocity of the flow that develops along time. However, in this problem there is a characteristic value for the flow velocity, namely the terminal speed of rise,  $v_{term}$ , given by the dynamical equilibrium between buoyancy and aerodynamic drag:

$$v_{term}^2 \sim \frac{\pi}{\gamma} \frac{\tilde{R}}{C_D} \frac{\Delta \rho}{\rho} c_s^2, \quad (10)$$

with  $C_D$  the customary drag coefficient,  $C_D \sim O(1)$ , and  $c_s$  the sound speed. Hence, the customary velocity-related parameters, like, e.g., the Mach num-

ber, the Reynolds number and the magnetic Weber number, can be immediately obtained as a function of the foregoing input parameters. For instance, using equation (5) we obtain that the Mach number must be of order:  $M^2 = O(\tilde{R}/\beta_0)$ . As a result, we expect the rise to be very subsonic and, assuming  $\tilde{R} \ll 1$ , sub-Alfvenic as well. This latter condition can be violated for tubes rising to higher levels of the convection zone.

The rest of this section is devoted to a discussion of the values expected for the most important parameters of this problem.

### 3.1. The amount of twist and the deformation of the tube

The central parameter for the present paper is the twist of the tube as measured by the pitch angle of the field lines,  $\Psi$ . The values of this parameter of interest for our calculation are those for which the transverse component of the field,  $\mathbf{B}_t$ , is able to suppress the conversion of the tube into a pair of vortex rolls. In the following we study different agents that tend to deform the tube. We come to the conclusion that the minimum value of  $B_t$  necessary to counteract them is the same for all.

#### 3.1.1. Differential buoyancy and pressure fluctuations along the boundary

The tube of the initial condition explained in §2.2 is increasingly buoyant toward its center. Thus, the central regions rise faster than the periphery; the upper layers of the tube are thereby compressed whereas those located below the center are expanded. The magnetic field lines are deformed by this process; the transverse field, in particular, exerts an increasing resistance against further deformation. One can calculate the minimum transverse field that can effectively withstand (and reverse) the buoyant deformation (Emonet & Moreno-Insertis 1996). At this point, it is sufficient to obtain an order of magnitude estimate for it that can serve as a guide for the rest of the paper. This can be easily done for tubes with smooth distributions like (6) and (8) or (9) and satisfying  $R^2 \ll H_p^2$ . The resulting criterion is best expressed in terms of the pitch angle calculated at the position of the maximum of the transverse field,  $\Psi_{mt}$ ; it reads:

$$\sin \Psi_{mt} \stackrel{\text{def}}{=} \left( \frac{B_t}{B} \right)_{mt} \gtrsim \tilde{R}^{1/2} \left( \left| \frac{\Delta \rho}{\rho} \right|_0 \frac{\beta_0}{2} \right)^{1/2}. \quad (11)$$

For the tubes with initial condition §2.2, this approximate criterion should hold within about a factor 2. A more precise condition involving the detailed buoyancy distribution in the tube can be obtained by studying the magnetostatic equilibrium of a horizontal twisted tube with a non-homogeneous buoyancy distribution in the limit  $R^2 \ll H_p^2$  (Emonet & Moreno-Insertis 1996). It can be shown (see their Eqs. 44 and 49) that for the deformation of the tube to remain small, the radial profile of the pitch angle,  $\Psi(r)$ , must satisfy:

$$\sin \Psi(r) \gtrsim \left( \frac{r}{H_p} \right)^{1/2} \left\{ \left| \frac{\Delta \rho(r) - \langle \Delta \rho \rangle(r)}{\rho(r)} \right| \beta(r) \right\}^{1/2}, \quad (12)$$

where  $\langle f \rangle(r)$  is the radial average of  $f$  between the radii 0 and  $r$ . At each radius  $r$ , the deformation of the magnetic field is directly related to  $\Delta \rho(r) - \langle \Delta \rho \rangle(r)$ , i.e., to the *differential buoyancy* at that radius.

The threshold due to the differential buoyancy (Eq. 11 or 12), however, cannot be the only criterion of interest for our problem. In fact, even a uniformly buoyant tube, if untwisted, is subjected to a deformation and conversion into vortex rolls. A deforming agent independent of the initial differential buoyancy is the pressure profile (i.e., the pressure fluctuations,  $p_{ef}$ , above the background stratification) built by the external flow around the boundary of the tube (Emonet & Moreno-Insertis 1996): a simple criterion for the resistance of the tube against those fluctuations is

$$\frac{8\pi|p_{ef}|}{B_t^2} \lesssim 1, \quad (13)$$

Now,  $p_{ef}$  is itself of order the ram pressure of the external flow relative to the tube. Thus, it is no higher than about  $\rho v_{term}^2/2$ . Substituting from Eq. (10), we obtain again a criterion as in (11).

#### 3.1.2. Vorticity generation

Given the central role of the vorticity in the present problem, it is adequate to understand the minimum condition (11) in terms of the vorticity generation. The time evolution of the longitudinal component of the vorticity,  $\omega_l$ , is governed by the following equation:

$$\begin{aligned} \rho \frac{D}{Dt} \left( \frac{\omega_l}{\rho} \right) &= \nabla \left( \frac{\Delta \rho}{\rho} \right) \times \mathbf{g} + \frac{\nabla \times \mathbf{F}_{L_t}}{\rho} \\ &+ \nabla \left( \frac{1}{\rho} \right) \times \left[ -\nabla \left( \Delta p + \frac{B_t^2}{8\pi} \right) + \mathbf{F}_{L_t} \right]. \end{aligned} \quad (14)$$

$\mathbf{F}_{L_t}$  represents the projection of the Lorentz force on the transverse plane  $(x, z)$ . For definiteness, when speaking about the sign of the vorticity in the rest of this section, we refer to the right half of the tube only.

At issue in this section is the generation of vorticity in the main body of the tube (the vorticity in the tube periphery is discussed in 5.2). The first term on the right hand-side is the counterpart in terms of vorticity of the gravitational torque: it produces *positive* vorticity because  $\nabla(\Delta\rho/\rho)$  points outwards. The second term on the right-hand side of (14) represents the effect of  $\mathbf{B}_t$  and can be rewritten as:

$$\frac{\nabla \times \mathbf{F}_{L_t}}{\rho} = \frac{(\mathbf{B}_t \cdot \nabla) \mathbf{J}_l}{c\rho}, \quad (15)$$

with  $\mathbf{J}_l$  the longitudinal component of the electric current density. At the beginning of the run, the longitudinal current is axisymmetric so that  $\nabla \times \mathbf{F}_{L_t}$  is zero. As soon as the tube center begins to rise relative to the periphery, the longitudinal current is enhanced in the upper half and diminishes in the lower half of the tube. According to Eq. (15), this produces *negative* vorticity in the interior of the tube, i.e., it tends to counteract the effect of the gravitational torque. By setting these two terms equal, we obtain a criterion for the minimum transverse magnetic field that can effectively oppose the initial deformation of the tube: the result is, again, (11). For the problem we are considering here, the last term of the vorticity equation (14) is  $O(\Delta\rho/\rho + L/\gamma H_p)$  smaller than the other two terms and is therefore not of primary interest here ( $L$  represents a local characteristic length for the transverse magnetic field, e.g., the radius of the tube or the thickness of the tube boundary).

Criteria equivalent to (11) can also be obtained through other physical considerations. For instance, Tsinganos (1980) obtained a similar threshold for  $\Psi$  by calculating the stability of the tube against splitting due to the development of Rayleigh-Taylor and Kelvin-Helmholtz instabilities at its apex.

## 3.2. Other parameters

### 3.2.1. Plasma beta and tube radius

The choice of values for the parameters  $\beta_0$  and  $\tilde{R}$  must be guided both by (astro)physical insight and feasibility of the numerical calculation.  $\beta_0$  is expected to be very high in the solar interior, like, e.g.,  $O(10^5)$  for the magnetic tubes at the bottom of the convection zone. The Courant condition for the numerical

code, though, sets a stringent upper limit to the value of  $\beta_0$  that we can use. Using expression (10) we can calculate the number of timesteps necessary for our tube to cross the whole integration box,  $n_t$ , as

$$n_t \gtrsim n_z \left( \frac{\beta_0}{\tilde{R}} \right)^{1/2}, \quad (16)$$

with  $n_z$  the total number of cells in the vertical direction. A trade-off between field intensity and magnetic flux of the tube is then necessary. As a compromise we have chosen  $\beta_0 = 10^3$  and  $\tilde{R} = 3.7 \cdot 10^{-2}$ . This should be sufficient to understand qualitatively the flows in and around the tubes with the field strength and flux expected in the progenitors of active regions.

### 3.2.2. The Magnetic Reynolds number, $Re_m$

The magnetic Reynolds number can be defined in this problem in terms of the terminal speed of rise and the tube radius. Its order of magnitude is thus given by  $Re_m = O(\tilde{R}^{3/2}/\tilde{\eta})$ . The choice of a value for this parameter must be guided primarily by numerical criteria: large magnetic field gradients develop in the tube along the evolution, specially at its upper rim. We have chosen the ohmic diffusivity so that the resulting value of  $Re_m$  is a few times  $10^2$ . This yields good numerical performance but causes some unwanted diffusion of the field outward from the tube. A measure for the latter can be obtained from the  $y$ -component of Walen's equation, obtained by combining the continuity and induction equations, (1) and (3):

$$\frac{D}{Dt} \left( \frac{B_l}{\rho} \right) = \left( \frac{\mathbf{B}}{\rho} \cdot \nabla \right) v^y + \frac{\eta}{\rho} \Delta B_l. \quad (17)$$

In the central region of the tube, the variation in  $B_l/\rho$  is basically due to diffusion. The calculations presented in the following are not diffusion-dominated (as expected from the high  $Re_m$ ), in the sense that the decrease of this quantity is small in the tube center during the period of time shown in the figures. This can also be checked through an order of magnitude estimate: the diffusion term in (17) for the initial gaussian distribution can be compared to the rate of change of the field (left-hand side of the same equation) imposed by the rise of the tube. The ratio between them is  $(Re_m \tilde{R})^{-1}$ , which is  $O(10^{-1})$  in the present case.

### 3.2.3. The Weber number, $We$

In the hydrodynamical literature on air bubbles,

Fig. 1.— Rise of a twisted tube through a stratified environment. The initial pitch angle  $\Psi_{mt}$  is  $7^\circ$ . The grey scale and the contours correspond to the longitudinal magnetic field intensity. At each time step white corresponds to the maximum of  $B_l$  at this instant and black to 1 percent of this maximum. The arrows correspond to the velocity field. In the figure, only a about 1/5 of the total integration box is reproduced; more precisely, 100 x 500 out of a total of 300 x 700 points for each half of the figure are included. The times represented are:  $t = 0, 1.3, 2.5, 3.8, 5.3, 6.6$ . The complicated shape of the wake in the two last panels is due to the episodic release of small secondary rolls

the Weber number is used to measure the relative importance of the inertial forces of the flow to the surface tension at the boundary of the bubble (e.g. Ryskin & Leal 1984b). The role of surface tension is played in our case by the jump in magnetic tension of the transverse component at the boundary of the tube. Hence we define the magnetic Weber number as

$$We \stackrel{\text{def}}{=} \frac{v^2 \rho}{B_t^2 / (4\pi)} . \quad (18)$$

Inserting for  $v$  the terminal speed we easily obtain  $We = \tilde{R} \beta_0 |\Delta\rho/\rho|_0 / (2 \sin^2 \Psi_{mt})$ . The condition on the minimum pitch angle to avoid the splitting of the tube, (11), can thus be reformulated as the condition that the *Weber number be at most of order one*,  $We \lesssim 1$ .

#### 4. The rise of a twisted tube in a moderately stratified environment: a representative case, $\Psi_{mt} = 7^\circ$

The critical value of the pitch angle parameter  $\Psi_{mt}$  obtained by substituting in (11) the chosen values of  $\beta_0$ ,  $\tilde{R}$  and  $\Delta\rho/\rho$  is  $6^\circ$ . In the present section we describe some major features of the rise of a tube with a pitch angle  $\Psi_{mt}$  close to that value,  $\Psi_{mt} = 7^\circ$ . The time evolution is illustrated in Fig. 1, which shows a fraction of the integration box used (30% and 70% of the box in the horizontal and vertical directions, respectively). In §7 we compare the results for flux tubes with different values of the initial  $\Psi_{mt}$ .

##### 4.1. The initial acceleration phase

In the absence of external flows to keep it in place, the tube lacks equilibrium globally and starts rising, at the same time sending out sound waves all across the box. The initial global acceleration is basically *free-fall*, i.e.,  $(g/i) (\overline{\Delta\rho}/\overline{\rho})$ , with an overbar indicating average values in the tube and  $i$  standing for the enhanced inertia factor, which turns out to be 2 (see §4.3.1).

Superimposed on the global rise, different kinds of motions within and around the tube take place which tend to deform its initial axisymmetric shape (Fig. 1, upper row). One of them is the faster rise of the tube center compared with the periphery due to the differential buoyancy (§3.1.1). As a consequence of this, the magnetic tension associated with the transverse field builds up at the tube front; the relative motion of the tube center is thus stopped and reversed. A

Fig. 2.— Distance to the stagnation point at the tube front of 50 mass elements initially located at equidistant points along the vertical symmetry axis as a function of time (solid lines). The compression of the tube front and the oscillations of the central regions along the vertical axis can be clearly seen. The curves plotted vertically (stars) are profiles of the transverse field intensity,  $B_t$ , along the vertical symmetry axis at regular intervals of time.

vertical oscillation of the tube center ensues within the tube's cross section. The compression/expansion in the upper/lower half of the tube together with the internal oscillations are clearly visible in Fig. 2, where we have plotted the position as a function of time of several Lagrange markers located along the vertical symmetry axis of the tube.

Simultaneously with the processes just explained, the external matter slides around the tube and *drags* toward the rear the outermost tube layers where the magnetic field is too weak to oppose any important Lorentz force. The field is thus stretched all along the boundary (§5). Vorticity is being generated in the matter being dragged: as a result, two magnetized vortex rolls are created that trail the tube motion (Fig. 1, third panel). The main body of the tube thereby loses about 30% of its original magnetic flux. This figure sensitively depends on the initial pitch angle (§7). Given the sign of the vorticity, the matter between the rolls is moving upwards with respect to the back of the tube. A pressure excess appears at the upper end of the inter-vortex space, directly below the lowermost tube layers.

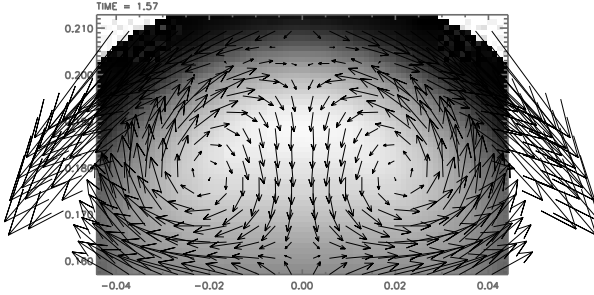


Fig. 3.— Close-up view of the tube interior showing the velocity vectors of the internal torsional oscillation. The arrows in the figure correspond to the relative velocity of the individual mass elements with respect to the tube apex.

#### 4.2. Torsional oscillations of the tube interior

The vertical oscillations of the tube center are in fact part of a torsional oscillation in which most of the tube interior is taking part (Fig. 3). The torsional oscillation has left-right symmetry: each tube half is rotating back and forth around a horizontal axis offset by a fraction of  $R$  from the midplane. The energy of this oscillation is being radiated away from the tube via pressure forces; it is also damped through the diffusion (physical and numerical) present in the code. Thus it slowly decreases in amplitude. The frequency of these oscillations is of order  $\omega_{tors} = O[v_{At}/(2\pi R)]$ . Hence, one expects a few torsional oscillations to be completed while the tube is rising across a scaleheight.

#### 4.3. The asymptotic regime of rise

The strong initial acceleration phase is followed by a quasi-stationary asymptotic regime (Fig. 1, lower row). In it, the rate of change of the tube interior and external flows becomes small compared with the initial phases. The transition occurs at about  $t = 3$  (between the third and fourth panels of Fig. 1). The asymptotic regime is characterized by the adoption of a terminal speed of rise, a sharp separation of tube interior and surroundings and a well-developed trailing wake. Simultaneously, the tube stops losing magnetic flux to the wake and there is no further important deformation of the magnetic field lines in the head of the tube. The following subsections deal with some of the features characterizing this asymptotic regime.

##### 4.3.1. The terminal velocity

Once the wake is developed, the resistance of the surroundings to the advance of the tube can be calculated using the customary aerodynamic drag force with almost constant drag coefficient  $C_D$ . In the asymptotic regime, the total buoyancy of the tube is a slowly varying quantity. Thus we can expect the tube to reach a terminal speed of rise given by:

$$v_{term} = \left( \frac{2gS\overline{\Delta\rho}}{C_D d \rho_e} \right)^{1/2}, \quad (19)$$

$S$  and  $d$  being the cross sectional area and horizontal diameter, respectively. The order of magnitude of this speed was estimated in Eq. (10). The best fit to the numerical results yields a value of  $C_D$  of approximately 1.6. The approach to this asymptotic regime is not immediate to formulate analytically, since the coefficient  $C_D$  is not constant while the tube is changing its shape and developing a wake. The initial acceleration of the tube as a whole is

$$a = \frac{g \overline{\Delta\rho}}{i \rho}; \quad (20)$$

the factor  $i$  allows for the added inertia due to the co-acceleration of the external medium ( $i = 2$  for a rigid straight cylinder). To approximate the velocity of the tube in the initial and intermediate time-dependent phases, we use the expression for a tube which starts from rest with acceleration  $a$ , is being acted upon by a constant driving force and has fixed  $C_D$ , viz.:

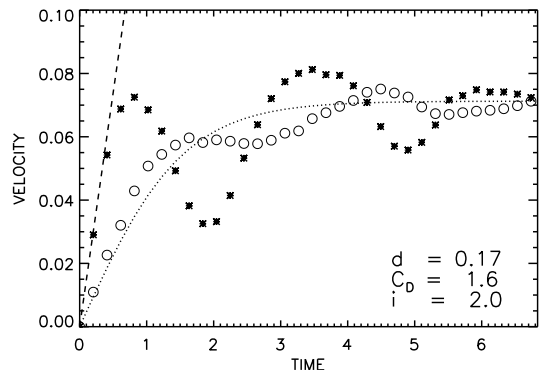


Fig. 4.— Velocity of the tube center (stars) and of the apex (circles) as a function of time. The dotted line corresponds to Eq. (21). The dashed line represents the initial acceleration of the tube center,  $(|\Delta\rho/\rho|)_{r=0} g/i$ , with  $i = 2$ .

a constant driving force and has fixed  $C_D$ , viz.:

$$v_{rise} = v_{term} \tanh \left( \frac{a t}{v_{term}} \right), \quad (21)$$

with  $v_{term}$  still given by Eq. (19).

The numerical results show a surprising closeness to Eq. (21). In Fig. 4, we show with a dotted line the velocity given by Eq. (21), while the actual speed of the tube apex,  $v_{apex}$ , is indicated as circles. As can be seen, the tube speed *oscillates* around the mean speed given by Eq. (21). This is due to the strong oscillations of the tube interior: in fact, the tube center oscillates with a much larger amplitude, as is shown by the curve with asterisks. The tube center *pushes* the apex, so that circles and asterisks are slightly out of phase. The amplitude of the oscillation diminishes as its energy is being radiated to the external medium and both curves converge toward the dotted line. The initial acceleration of the tube apex is very close to (20) with  $i = 2$ , i.e., as corresponds to the global buoyancy of the tube. The tube center, in turn, has a higher acceleration, corresponding to the local value of the buoyancy, namely  $(|\Delta\rho/\rho|)_{r=0} g/i$  (this value is shown in the figure as a dashed line). Here again, the enhanced inertia factor  $i$  must be set equal 2.

As a test to the validity of the terminal velocity formula, we have calculated the evolution of tubes starting with the same initial condition as the one used to obtain Fig. 4 (in particular, the same tube radius,  $R$ ) but with  $\beta_0$  chosen in a range between 1000 and 100. The velocity curves of all these tubes are similar to those shown in Fig. 4, with the time scale contracted by a factor  $\beta_0^{1/2}$  and the velocity scale enlarged by the same factor. More precisely, if all these tubes reach the aerodynamic drag regime with terminal velocity given by Eq. (19), then the curves depicting the velocity of the apex normalized by the plasma beta,  $v_{apex}\beta_0^{1/2}$ , versus the position of the apex must all basically coincide (the drag coefficient  $C_D$  does not change much with varying Reynolds number in this regime). The results of the tests show indeed a large degree of superposition of those curves: the maximum relative deviation between them is a factor 1.1, which can be attributed to the change in  $C_D$  consequent with the variation in the Reynolds number.

#### 4.3.2. The equipartition line at the tube periphery

As a result of the resistance to deformation provided by the transverse field, there is a neat separation between the tube interior and the outside in the asymptotic regime. A good indicator of the location of the tube boundary can be obtained by comparing the kinetic energy density of the relative flow field,  $\mathbf{v}_{rel} \stackrel{\text{def}}{=} \mathbf{v} - \mathbf{v}_{apex}$ , viz.  $e_{kin} \stackrel{\text{def}}{=} \rho v_{rel}^2/2$ , with the energy density of the transverse magnetic field,  $e_{mag} \stackrel{\text{def}}{=} B_t^2/(8\pi)$ . We define the *equipartition line* as the locus of those points in the tube periphery where the two energy densities are equal. Fig. 5 shows, at time  $t = 3.8$ , the relative flow field  $\mathbf{v}_{rel}$  and, superimposed on it, the equipartition line. The flow field changes markedly when going across the equipartition line: the velocities inside are much smaller than outside it. In other words, once the terminal velocity has been reached the tube rises basically as a unity, with only a weak internal flow pattern corresponding mainly to the torsional oscillations described in the previous section. A comparison of Fig. 5 with the results of laboratory experiments (e.g., Collins 1965 or plate 15 in Batchelor 1967), shows that there are

Fig. 5.— Equipartition line at  $t = 3.8$  together with the flow field relative to the apex of the tube. The simple structure of the wake at this time is clearly visible. The envelope of tube and wake has a well defined elliptical shape. This figure bears a strong resemblance to the experimental results of air bubbles rising in liquids (e.g., Collins 1965, also reproduced by Batchelor 1967, plate 15).

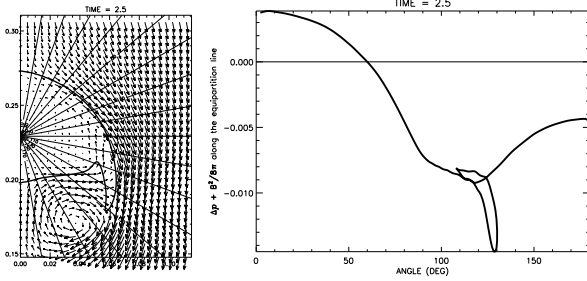


Fig. 6.— Profile of the total pressure excess along the boundary of the tube, which is defined by the equipartition line (see §4.3.2), at time  $t = 2.5$ . The boundary of the tube (the equipartition line) is shown as a thick line in the left panel. The feature in the middle of the profile (between  $110^\circ$  and  $130^\circ$ ) results from the shape of the equipartition line at the lateral edge of the tube. The arrows on the left panel correspond to  $\mathbf{v}_{rel}$  and the radial lines are drawn at constant azimuthal angles.

striking similarities between buoyant magnetic tubes and air bubbles rising in a liquid, both in the shape of the rising object itself as in the wake, in spite of the very different parameter values involved (like, e.g., the density deficit).

All along the initial phase, a pressure profile is set up around the tube periphery which closely resembles the pressure distribution around rigid cylinders in relative motion with the surroundings. To show this, we can plot (Fig. 6) the pressure in the points along the equipartition line. In this figure, the pressure excess associated with the return flow between the vortex rolls of the wake is clearly visible.

## 5. The sharp interface at the tube boundary: magnetic boundary layer

All around the equipartition line there is a region with non-zero vorticity. This contains (1) a boundary layer surrounding the tube and (2) the trailing wake. Further out, there is the external medium with a largely vorticity-free flow. In this section we study the structure of the boundary layer; the wake is considered in §6.

The two main physical features characterizing the magnetic boundary layer around the tube are a strong shear of the tangential flow and high magnetic field gradients. They lead to enhanced generation of vorticity, ohmic diffusion and generation of entropy. In

the following subsections we study these items in turn:

### 5.1. Shear flow and field gradients

A pronounced shear is taking place in a thin band around the equipartition line (Fig. 5). As a result, the matter elements and the transverse field are being stretched at the tube periphery all around the tube. To visualize this phenomenon, we use *Lagrange markers* which follow the motion of the tube's mass elements (Fig. 7). We choose six groups of markers at time  $t = 0$  (left panel), at a distance of the tube center such that  $B_l$  is 5% (white asterisks), 27% (black triangles) and 77% (black diamonds), respectively, of  $B_{l0}$  (the maximum value of  $B_l$  in the tube) both in the upper and lower half of the tube. The markers are set in the neighborhood of the tube axis and are left to evolve with the tube. As time advances, the markers of the outermost group in the upper tube half are stretched by a very large factor along the tube periphery (center and right panel of the figure); in fact, many of them are brought all the way down to the wake. The markers of the group immediately below them (triangles) are brought close to the uppermost group and stretched, albeit by a smaller factor than the other group. Large compression and stretching happen basically only in the neighborhood of the interface between tube and surroundings: closer to the tube center (diamonds) the mass elements are just periodically moved following the internal torsional oscillation. At the rear of the tube, the Lagrange markers with  $B_l = 0.27 B_{l0}$  (triangles) are also somewhat stretched by the flow of the trailing wake (see §6). The outermost parcels at the back of the tube (white asterisks) are trapped in the tail and no longer rise with the tube.

Corresponding to this shearing, the pitch angle increases to large values at the tube periphery: in Fig. 8 we plot the pitch angle distribution along the vertical axis of symmetry for the three instants shown in Fig. 7. The pitch angle becomes large in the interface at the tube front (middle panel). In the quasi-stationary regime, its distribution shows a horizontal asymptote outside the tube similar to the one of the initial condition. This feature is *not* a mere consequence of our initial condition (8). In fact, an initial pitch angle distribution with exponential decline for large radius at time  $t = 0$  (see Eq. 9) yields in the quasi-stationary regime a horizontal asymptote similar to the one of Fig. 8. It is then perhaps more natural to choose the initial condition of Eq. (8) from

Fig. 7.— Motion of individual mass elements in the tube, showing the stretching of the matter and field along the tube boundary. The panels correspond to  $t = 0, 1.9$  and  $3.8$ . At time zero the Lagrange markers are located at  $R/H_p = 0.044$  and  $0.068$  where  $B_l$  is equal to  $27\%$  and  $5\%$  of its value at the center. Radial compression, azimuthal stretching and shearing of the upper layers of the tube is apparent. The elements indicated by black triangles at the back are also somewhat stretched as a result of flow in the wake.

the outset.

The large pitch angles apparent on the right of Fig. 8 are all in a region of the tube where the magnetic field intensity is very low; the central regions, on the other hand, have low pitch angles. Thus, one should not expect a global kink-unstable behavior of the tube. This can be checked by calculating the net tension in the tube over background (see §9.2 in Parker 1979). With the convention that tension is positive and pressure negative, we obtain a positive value indicating that the tube is under longitudinal tension rather than compression. Thus, there should be no tendency to buckling of the tube.

## 5.2. Vorticity generation in the boundary layer

The large jump in tangential speed visible across the equipartition line in Fig. 5 marks the presence of a *vortex sheet* surrounding the tube. In fact, vorticity (more precisely, its longitudinal component  $\omega_l$ ) is generated at the boundary layer during the whole

duration of the run. From there, it is advected toward the wake.

These processes are governed by Eq. (14). As in §3.1, the right-hand side is dominated by the first two terms [the third is again  $O(1/\beta_0)$  smaller]. However, along the front of the tube those two terms, i.e., the gravitational and magnetic vorticity sources, *reinforce each other* rather than mutually cancel, as in the tube interior. This is because the radial derivative of the transverse field component reverses its sign in the neighborhood of the equipartition line. For instance, in the simple case in which the field lines are still not far from circular (e.g., along the front) the magnetic contribution is approximately,

$$\frac{\nabla \times \mathbf{F}_{L_t}}{\rho} \cong \frac{B_t}{c \rho} \frac{\partial}{\partial \phi} \underbrace{\left[ \frac{1}{r} \frac{\partial}{\partial r} (r B_t) \right]}_{\cong J_l}, \quad (22)$$

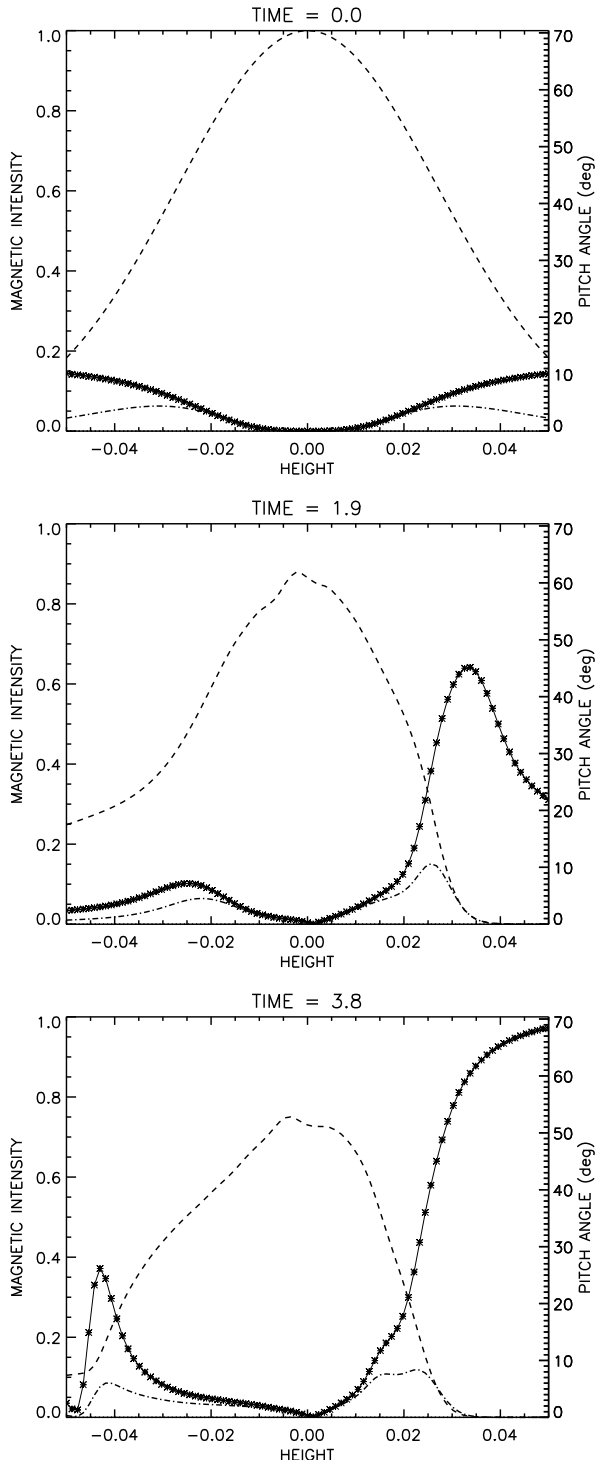


Fig. 8.— Pitch angle distribution (stars) along the vertical central axis at three different times corresponding to the 3 panels of Fig. 7. The profiles of  $B_l$  (dashed) and  $B_t$  (dotted-dashed) are overplotted.

so that  $J_l$  changes sign at about the maximum of  $B_t$ . As a result, (and taking into account the sign of the azimuthal derivative  $\partial/\partial\phi$ ), in the right half of the tube positive vorticity is generated all along the front of the tube, and negative vorticity is generated at the rear, i.e., at the interface between the tube and the wake. At the rear  $\nabla(\Delta\rho/\rho)$  is approximately parallel to  $\mathbf{g}$  and therefore the magnetic stress is anyway the main source of vorticity there.

In Fig. 9 we show the distribution of vorticity in the box at four different times during the evolution. White and black indicate positive and negative vorticity, respectively (i.e., clockwise and anticlockwise rotation), whereas the grey background is the zero vorticity level. Soon after the beginning (leftmost panel;  $t = 0.3$ ) the gravitational torque is creating positive and negative vorticity in the right and left tube halves, respectively, across the whole tube interior. In the second panel ( $t = 1.6$ ), this has already been countered by the magnetic tension of the transverse field: the reversal of the sign of the vorticity in the interior reveals the first backward torsional oscillation. Additionally, a vortex sheet is already apparent all around the tube front. At the rear, there is only an incipient wake and no clear vortex sheet yet. The third and fourth panels correspond to the asymptotic phase ( $t = 3.8$ , i.e., close to the beginning of the stationary regime, and at an advanced stage,  $t = 5$ , respectively). Vorticity generation now occurs basically close to the equipartition line only. Vortex sheets along *both* the front and the rear of the head of the tube are visible. As expected, the sign of the vorticity in them is opposite. A detailed distribution of  $\omega_l$  in the boundary layer around the tube (from top to bottom), can be seen in Fig. 10. The vorticity indeed changes sign at the edge of the tube: the abrupt shape of the zero crossing is due to the acute shape of the latter. The small maximum at the right end of the distribution is characteristic of the tail (§6.2).

### 5.3. Ohmic diffusion and field advection

The structure of the magnetic boundary layer is dominated by the ohmic diffusivity, which in part plays in the present case the role of the viscosity in the standard hydrodynamic boundary layers. An important difference between viscous and purely magnetic boundary layers, though, concerns the no-slip condition for the flow: in the purely magnetic case, there is no counterpart to the viscous second-order derivative term that could force the tangential veloc-

Fig. 9.— Distribution of the  $y$ -component of the vorticity vector in and around the tube at  $t = 0.3, 1.6, 3.8$  and  $5.0$ . White corresponds to positive vorticity (clockwise rotation) and black to the opposite. The two leftmost panels clearly show the vorticity associated with the torsional oscillations. The boundary layer and vortex sheet at the tube front are visible in the three rightmost panels. In the two last panels the vortex sheet at the interface between the wake and the tube is also visible.

ity to reach a zero value at the boundary. In our case, however, the flows on the inner side of the equipartition line are reduced or suppressed by the magnetic forces. In other words, in the present boundary layer the Lorentz force imposes a *no-slip* condition which does not allow a penetration of the external incoming flow into the tube nor large fluctuations of the transverse velocity inside. This is clearly visible in Fig. 11 where we have plotted  $v_x$ ,  $(v_{rel})_z$ ,  $B_t$  and  $B_l$  along a vertical axis slightly offset from the symmetry axis.

The slope of the profile of  $B_t$  and  $B_l$  across the boundary layer results from the equilibrium between the outward ohmic diffusion and the field advection through the external flow. For  $B_t$ , for instance, this is controlled by the transverse component of the induction equation (Eq. 3). Written in terms of the magnetic potential  $A$ , the latter reads:

$$(\mathbf{v}_{rel} \cdot \nabla) A = \eta \Delta A, \quad \text{with} \quad \mathbf{B}_t \stackrel{\text{def}}{=} \nabla \times (A \mathbf{i}_y). \quad (23)$$

As the transverse field diffuses outward, it *swallows*

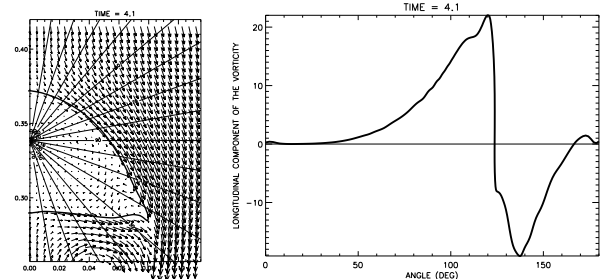


Fig. 10.— Profile of the longitudinal component of the vorticity (right panel) along the equipartition line drawn in the left panel for  $t = 3.8$ . The zero crossing at about  $120^\circ$  corresponds to the transition from tube front to rear at the edge of the tube. The radial lines in the left panel are drawn at constant azimuthal angles.

some of the incoming external matter (which, in this way, slowly enters the magnetic field system). Simultaneously, this same external matter *advects* the magnetic field back toward the tube interior. The equilib-

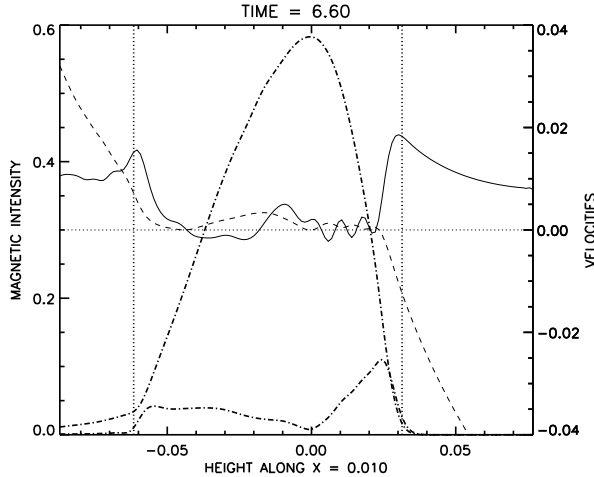


Fig. 11.— Plots of  $B_l$  and  $B_t$  (dash-dotted) together with  $v_x$  (solid line) and  $(v_{rel})_z$  (dashed) along a vertical axis at  $x = 0.01$ . The vertical dotted lines correspond to the positions where  $e_{mag_t} = e_{kin}$ .

rium between those two terms is reached for a given thickness of the boundary layer,  $L_{bl}$ . To obtain an estimate for  $L_{bl}$ , we note that the external flow has a lengthscale comparable with the tube radius (a common feature of cylinders moving in fluid media), so that,

$$L_{bl} \sim \frac{R}{Re_m^{1/2}}. \quad (24)$$

This estimate is in agreement within a factor about 2 with the results of the numerical calculation (see Fig. 11). An analogous advection-diffusion equilibrium can be seen to hold for  $B_l$  in the boundary layer.

#### 5.4. Comparison with air bubbles and rigid tubes.

In spite of the striking similarities between the present problem and the rise of an air bubble, the corresponding boundary layers at the periphery of the rising object differ in important ways. The boundary of an air bubble is basically a *free surface* for the external medium, since the density and viscosity in the interior are negligible compared with those outside. The external flow must then satisfy a zero tangential stress boundary condition rather than the no-slip condition of the present magnetic tube (e.g., Batchelor 1967, §5.14; Ryskin & Leal 1984a, 1984b). As a consequence, the tangential velocity at the gas/liquid

interface in the air bubble does not vanish, but must instead satisfy the following equation:

$$\omega_l = 2\kappa(v_{rel})_{tg}, \quad (25)$$

with  $\kappa$  the curvature of the boundary layer and  $(v_{rel})_{tg}$  the tangential component of the relative flow speed. The resulting jump in tangential velocity across the boundary layer of a bubble is therefore only of order  $Re^{-1/2}$ , while it is  $O(1)$  for a no-slip boundary layer, as in the present problem.

The magnetized boundary layer of the rising tube, in fact, resembles more closely the boundary layers around solid bodies with a no-slip condition than those around air bubbles. The distribution of vorticity along the equipartition line shown in Fig. 10 is quite similar to that around the boundary of a rigid cylinder at  $Re \cong 300$  (e.g., Ta Phuoc Loc 1980). In our case, though, the reversal of the sign occurs more abruptly because of the particular geometry of the equipartition line.

#### 5.5. Entropy generation

The enhanced ohmic dissipation in the boundary layer is creating entropy at a rate:

$$\frac{D}{Dt} \left( \frac{\Delta s}{c_p} \right) = \eta \frac{\gamma - 1}{\gamma} \frac{(\nabla \times \mathbf{B})^2}{4\pi p}, \quad (26)$$

To order of magnitude, this entropy increase can be written:

$$\frac{D}{Dt} \left( \frac{\Delta s}{c_p} \right) \approx \frac{1}{\beta_{bl}} \frac{v_{rise}}{R}, \quad (27)$$

with  $\beta_{bl}$  the local plasma beta in the boundary layer. The entropy increase for a matter element moving all along the tube boundary is then of order  $1/\beta_{bl}$ . As a result, the density difference  $\Delta\rho/\rho$  of those elements can be substantially modified. This, however, is unlikely to cause important modifications in the dynamical behavior of the tube boundary. The main driving force there, the pressure gradient, is of order  $\rho v_{rise}^2/R$ ; therefore, it should be more important than the local gravitational term  $g\Delta\rho$  by the ratio  $B_0^2/B_{bl}^2 \gg 1$ , where  $B_{bl}$  is the magnetic field strength in the boundary layer.

In our numerical simulation we also have some increase of entropy due to the artificial viscosity. Its influence, however is only secondary because of the low value of  $Re_m$  chosen.

## 6. The wake

Wakes have been the object of active research in fluid dynamics for at least the past four decades. This includes the wake behind solid cylinders (e.g., Collins & Dennis 1973a; Collins & Dennis 1973b; Ta Phuoc Loc 1980, Bouard & Coutanceau 1980; Ta Phuoc Loc & Bouard 1985), drops (Dandy & Leal 1989; Stone 1994) and air bubbles (Davies & Taylor 1950; Collins 1965; Parlange 1969; Wegener & Parlange 1973; Hnat & Buckmaster 1976; Ryskin & Leal 1984b; Christov & Volkov 1985). In this chapter we briefly describe the formation and structure of the wake behind the rising magnetic tube and pay special attention to the similarities and differences to other wakes known in the literature.

### 6.1. The time evolution of the wake

Solid cylinders, air bubbles and drops have a clearly defined boundary from the beginning. Vorticity is created along the boundary and advected downflow. The wake is formed out of external fluid only, via, e.g. in solid bodies, the detachment of the boundary layer. In our case, in contrast, there is no such clear boundary at the beginning. The layers of weak magnetic field in the outskirts of the tube (a) are unable to resist the incipient external flow so that they are bodily convected to the rear and (b) increase their vorticity through the mechanisms explained in §3.1.2 and §5.2. It is the accumulation of this rotating material at the back of the tube that constitutes the wake. The material making up the wake may in fact be a large fraction of the initial tube in the case of small initial pitch angles (§7).

The process of formation of the wake is basically complete by  $t = 3.0$  (see Figs. 1 and 5) and this signals the transition to the asymptotic regime of rise (§4.3). The latter, however, is not exactly stationary, since the wake does not remain unmodified in the rest of the evolution. In fact, it slowly grows in size and episodically changes its shape. The growth can be seen in Fig. 12, where the vertical size of the rolls is depicted as a function of time. The elongation is roughly linear, with a small-amplitude oscillation superimposed. This kind of behavior is not unknown in fluid dynamics. The elongation of the wake is indeed similar to what is observed behind a rigid cylinder moving at constant speed with  $R_e \cong 300$  after an impulsive start (see Ta Phuoc Loc 1980): in the laboratory experiment the linear growth of the wake

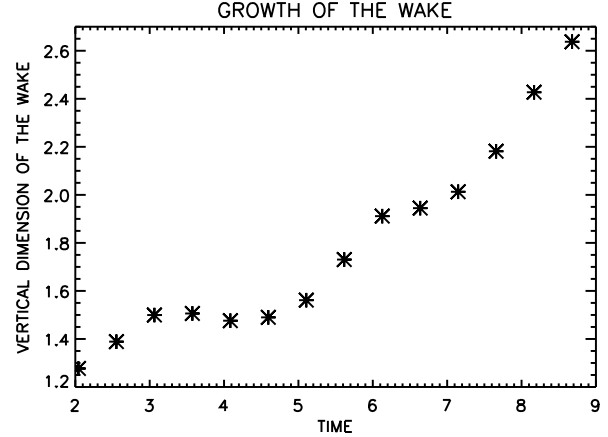


Fig. 12.— Vertical size of the wake as a function of time, calculated as the distance between the stagnation point at the rear of the tube and the stagnation point at the bottom of the wake. The growth is quasi-linear, with oscillations superimposed.

with time continues well after the high- $R_e$  flows have been set up around the cylinder and  $C_D$  has reached a constant value close to 1. For higher values of  $R_e$  ( $= 3000$ ) the growth of the wake with time is exponential rather than linear (Ta Phuoc Loc & Bouard 1985). In our case, a small part of the growth of the wake is due to the stratification; however, its main cause is the transport of rotating material from the boundary layer along the boundary of the tube to the wake. This is clearly visible in the third and fourth panels of Fig. 9: a white *streamer* of positive vorticity coming from the tube front is being wrapped up first around and then into the roll on the right-hand side of the wake. Simultaneously, a black *tongue* with origin in the back of the tube is also making inroads into the wake, next and following a parallel path to the white streamer.

In the case of rigid tubes and bubbles moving through a fluid (and assuming perfect symmetry about the object's midplane), the growth of the wake normally lasts until a dynamical equilibrium is adopted. In it, the vorticity generated in the boundary layer is advected to the wake, where it is redistributed through viscous diffusion and further advection. Simultaneously, the energy gained through the driving force (the potential energy for the bubbles) is transformed into heat in the wake, again through viscous dissipation (Parlange 1969; Wegener & Parlange 1973). Further changes may occur if there is no mech-

Fig. 13.— Formation and release of a secondary roll at the edge of the tube. The panels contain a time series showing the equipartition line and the relative flow field. The secondary roll is being released to the downflow; later on, it gets dragged all around the wake and noticeably perturbs the shape and velocity distribution of the latter. Note also the jumps in velocity inside the main roll of the wake, revealing the presence of vortex sheets which have been advected from the tube front.

anism to dispose of the heat thus generated.

In the results presented here, no dynamical equilibrium is reached since there is no equivalent mechanism to diffuse the vorticity effectively. This can be seen quantitatively as follows: the characteristic time for the adoption of a stationary state in the wake through viscous diffusion and dissipation is  $Re (L_{\text{wake}}/R)^2$  times longer than the characteristic time for the formation of the wake itself,  $L_{\text{wake}}$  being the transverse dimension of the wake and  $Re$  the viscous Reynolds number. In our case,  $L_{\text{wake}} \approx R$  and we expect  $Re$  (e.g., calculated on the basis of the numerical viscosity) to be at least as high as  $Re_m$ . Therefore, the establishment of the dynamical equilibrium lasts much longer than the evolution presented in this paper. The consequence of this is the very inhomogeneous vorticity distribution apparent in Fig. 9. In a high- $Re$  case, in fact, it may never come to a full dynamical equilibrium because an instability interrupts the approach to a steady state: the two standing rolls develop asymmetric oscillations until one of them is released downstream (see, e.g., Batchelor 1967, plate 10). In contrast, in low- $Re$  bubble experiments, the trailing vortex rolls are similar to a Hill's vortex (e.g., Collins 1965; Parlange 1969; Wegener & Parlange

1973; Ryskin & Leal 1984b; Christov & Volkov 1985).

## 6.2. Further structural features common with laboratory experiments.

### 6.2.1. The skirt

In experiments with buoyant air bubbles, it is often observed that a small quantity of air is torn off (or sucked from) the bubble corner and becomes stretched all around the wake. The result, commonly called the *skirt*, is a sheet of air aligned with the interface between the wake and the external medium, which remains attached to the bubble (e.g., Hnat & Buckmaster 1976). A similar feature can be identified in our numerical simulations coinciding with the streamers or tongues of vorticity of both signs mentioned in the last section. In contrast to the air bubbles, the *skirt* here is made of magnetized material. During the whole rise the magnetic field in the skirt is continuously compressed and stressed both by the wake and external flows.

Fig. 14.— Tube and wake structure for four cases with different initial pitch angle but otherwise equal initial conditions. From left to right, the values of  $\Psi_{mt}$  were  $13.9^\circ$ ,  $7^\circ$  (i.e., the case studied in the rest of the paper),  $2.5^\circ$  and  $0^\circ$ . The lower panels show the general flow field and the contours of magnetic intensity for  $B_l$ . The upper panels represent the velocity relative to the apex of the tube and the corresponding equipartition line (as defined in §4.3.2). The transition from a convex tube back to a flat and then to a concave one for decreasing initial  $\Psi_{mt}$  (i.e., as the Weber number increases) is apparent. In the untwisted case, no *head* is left but, rather, a bridge joining the

### 6.2.2. The tail

All along the central symmetry plane, the rising tube is leaving behind a *tail* of weakly magnetized matter (Fig. 1). Its upper part is compressed by the two rolls of the wake. In fact, the *tail* is not only magnetized, but also has non-zero vorticity. This can be seen both in the distribution of Fig. 10 (maximum of positive vorticity at the right end of the figure) and, as a light shadow, in the vorticity map of Fig. 9. Similar structures are seen behind moving pair of vortices as well as in bubble experiments (e.g. Wegener & Parlange 1973). The total amount of magnetic flux which is lost by the tube to the tail is small (only 6 percent of the total flux).

### 6.2.3. The secondary rolls at the edge of the tube

Close to the lateral edges of the tube (see Fig. 13 and the last panel in Fig. 9) small secondary rolls are built from time to time; they grow for a while and then they are released to the downflow. These features are reminiscent of the secondary rolls observed near the detachment point of boundary layer around solid cylinders (Ta Phuoc Loc 1980; Ta Phuoc Loc & Bouard 1985). These secondary rolls strongly perturb the skirt and the wake when they are released: this is the main cause for the irregular shape of the wake in the last panel of Figs. 1 and 9.

## 7. The rise of tubes with different initial degrees of twist

The initial value of  $\Psi_{mt}$  for the tube whose rise we have described in the foregoing chapters was close to the value given by the criterion (11), namely  $\Psi_{mt} = 6^\circ$ . This criterion provides a lower bound for the twist necessary to withstand the destruction of the tube through vorticity generation in its interior, external pressure forces, etc; we do not know yet how sharp that bound is. In the present section we investigate the transition from the low-twist to the high-twist regimes. We conclude that the change from one to the other is gradual and takes place over a range of, say, 5 degrees in  $\Psi_{mt}$ , around the value given by the right hand side of Eq. 11. In Fig. 14 we show the relative flow,  $\mathbf{v}_{rel}$  (upper panels) and the contours of longitudinal magnetic intensity,  $B_l$  (lower panels), for four cases with  $\Psi_{mt} = 13.9^\circ, 7^\circ, 2.5^\circ$  and  $0^\circ$ , respectively. There is a clear gradation of properties and evolutionary patterns along the four columns of the figure. The amount of flux remaining in the *head*

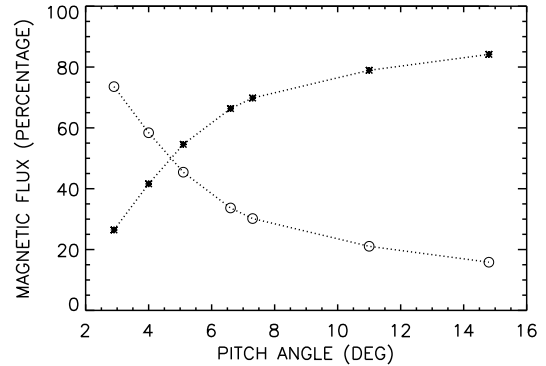


Fig. 15.— Percentage of the initial magnetic flux remaining in the head of the tube once the terminal velocity has been reached (stars) as a function of  $\Psi_{mt}$ . Shown is also the percentage of flux that has been dragged to the wake (circles).

of the tube is an increasing function of  $\Psi_{mt}$ . This can be seen in Fig. 15: the stars, representing the percentage of the initial flux which remain in the head, go from more than 80% for  $\Psi_{mt} = 13.9^\circ$  to about 20% for  $\Psi_{mt} = 2.5^\circ$  and (trivially) 0% for  $\Psi_{mt} = 0^\circ$ . In this figure, the change between the two regimes occurs between, say,  $3^\circ$  and  $8^\circ$ .

Not only the size, but also the shape of the remaining head varies markedly from one case to the other (Fig. 14, upper panels). For  $\Psi_{mt} = 13.9^\circ$ , the tube maintains its roundish shape all along. This is specially striking at the rear of the tube: the rising return flow between the two rolls in the wake cannot dent the back of the tube. This case is closest to the motion of a rigid cylinder in a fluid. For  $\Psi_{mt}$  decreasing down to  $2.6^\circ$ , the back of the tube becomes first flat and then concave through the action of the return flow. This transition coincides with the increase of the magnetic Weber number up across unity:  $We$  is 0.19, 0.74 and 5.75 for  $\Psi_{mt} = 13.9^\circ, 7^\circ$  and  $2.5^\circ$ , respectively. In the untwisted case, there is no longer a neat separation between tube interior and external flows. The rolls in the wake now contain 70% of the original magnetic flux, with most of the rest contained in the upper arch linking them. The evolutionary pattern in this case is similar in many respects to the results of Longcope et al. (1996).

Further insight into the structural differences for the tubes of Fig. 14 can be obtained by comparing

now the distribution of  $e_{mag_t}$  along the vertical axis at times  $t = 0$  (upper panel) and  $t = 5$  (lower panel), divided in both cases by the kinetic energy density at the upper stagnation point of the tube in the asymptotic regime,  $e_{kas}$  (calculated in the figure at time  $t = 5$ ). In the case with the highest  $\Psi_{mt}$  (dashed line), at  $t = 0$  only a thin skin at the outermost tube boundary is below the terminal kinetic energy level; we expect a skin of roughly that size to be dragged to the wake. For  $\Psi_{mt} = 7^\circ$  (solid line) and  $\Psi_{mt} = 2.5^\circ$  (dotted line), most (or all) of the tube at time  $t = 0$  has  $e_{mag_t}$  below the  $e_{kas}$  level. However, in the initial phases of the evolution the transverse field is substantially intensified through the compression and stretching phenomena explained in §4. This allows the *head* of the tube to be formed and its energy  $e_{mag_t}$  to be at (or above) the  $e_{kas}$  level in the asymptotic regime (Fig. 16, dotted line in the second plot).

## 8. Discussion

The results presented in this paper can be discussed from a twofold perspective. First, they can be applied to the theory of the magnetic activity in the Sun, trying to understand different aspects of the rise of magnetic flux across the convection zone. On the other hand, the simulations described here bear a strong resemblance to the results of laboratory and numerical experiments on the motion of air bubbles and rigid cylinders; it would be as well to clarify similarities and differences. The following subsections discuss different aspects of those topics.

### 8.1. The parameters and distribution of basic physical variables

The numerical calculation of the present paper is necessarily idealized. The calculations were done in a high-beta regime with small ratio of radius to pressure scaleheight. In thus far, they are within the parameter regime of expected for the magnetic tubes in the deep convection zone. The latter have a larger  $\beta$ , by a factor between 10 and 100, than adopted here but many qualitative features of the rise should be similar in both cases. The only diffusive process considered, though, the ohmic resistivity, together with the numerical viscosity and diffusion, yield laminar flows in and around the tube with Reynolds number of a few hundred. This cannot be expected to hold in the actual Sun: there, the rise of the tube will be accompanied by turbulent flows (with, in particular,

Fig. 16.— Initial and asymptotic profiles of the distribution of magnetic energy in the transverse field,  $e_{mag_t}$ , along the vertical axis of symmetry compared, in both cases, with the asymptotic kinetic energy density  $e_{kas}$  at the apex of the tube. The asymptotic values were calculated at  $t = 5$ . The different curves correspond to cases with initial pitch angle  $\Psi_{mt} = 13.9^\circ$  (dashed),  $\Psi_{mt} = 7^\circ$  (solid) and  $\Psi_{mt} = 2.5^\circ$  (dotted).

the energy density of the transverse field,  $e_{mag_t}$  with the kinetic energy reached asymptotically by the head of the tube. The order of magnitude of the latter is  $(Bl^2/8\pi)\bar{R}(1 + \tan^2\Psi)$ . This varies little (about 6% only) between  $\Psi_{mt} = 2.5^\circ$  and  $\Psi_{mt} = 13.9^\circ$ . The magnetic energy of the transverse field, in contrast, varies by a large factor (approx. 30) between those two extremes. For the comparison (Fig. 16), we plot

a turbulent wake).

In spite of the foregoing, a conclusion seems unavoidable: for the transport of the magnetic flux to the surface in the form of buoyant magnetic flux tubes to be effective, the latter must be twisted from the early stages of their rise. We have shown for a tube with a density deficit of order the full isothermal value ( $\Delta\rho/\rho \sim -1/\beta$ ) that an average pitch angle around  $\sin^{-1}[(R/H_p)^{1/2}]$  is indeed necessary for the tube to withstand the various deforming agents. Otherwise, they lose most of their magnetic flux to the trailing wake. As shown by earlier authors, the vortex rolls of the wake can easily end up moving horizontally rather than rising. The condition on the minimum pitch angle may be less stringent, though, if we consider that the rise may actually be driven by the Parker instability in tubes which are stored in a neutrally buoyant equilibrium (Caligari et al. 1995). The instability occurs with the upgoing mass elements being driven by a vertical force which remains well below  $\rho g/\beta$  while the amplitude is not too large. To a driving force of amount  $f \rho g/\beta$  ( $f \ll 1$ ) corresponds through (11) a minimum pitch angle which is about a factor  $f^{1/2}$  smaller than for isothermal straight tubes. For example, in the case discussed in the paper of Caligari et al. 1995,  $f < 0.04$  for the top of the rising loop in the lowermost 10,000 km of the rise, i.e., for distances equivalent to about 5 times the tube radius.

Even if the tubes are strongly buoyant [ $|\Delta\rho/\rho| = O(1/\beta)$ ] from the beginning, their time evolution may depend to some extent on the precise distribution of the density deficit in the tube at time  $t = 0$ . A gaussian profile, as used in this paper, yields a fast deformation of the initial magnetic configuration, followed by internal torsional oscillations. This is directly associated with the torque of the buoyancy force throughout the tube interior. A top-hat profile ( $\rho_i < \rho_e$  but  $\Delta\rho = \text{const}$ ), on the other hand, has no buoyancy torques associated except at the tube boundary. Yet, the time evolution of such a tube for smooth pitch angle distributions like (8) or (9) is qualitatively similar to the cases studied in this paper, as has been tested through a series of numerical experiments. This can be understood in different ways: first, the hydrodynamic forces associated with the external flow depend on the speed of rise of the tube, which is a function of the average buoyancy rather than of the precise shape of the  $\Delta\rho$  profile. To counteract them, one needs to have a sufficient pitch angle in the tube interior. On the other hand, the gravitational term in the vortic-

ity equation (14) for a top-hat profile is concentrated at the periphery of the  $\Delta\rho$  distribution, but is correspondingly more intense. To counteract it, it is necessary to have a large current density  $J_l$ , which can only be achieved if  $B_t$  is sufficiently intense, at least close to the tube boundary. Through both arguments one arrives at criteria basically like Eq. (11).

## 8.2. Twisted tubes in the convection zone: three-dimensional effects

If the magnetic tubes that yield active regions at the surface must be twisted already in the early stages of the rise, the Sun should have a mechanism to routinely produce twisted tubes in the dynamo layers. If one relaxes the condition of symmetry along the tube imposed in the present paper, one may think that the twist could result through torsional shearing. This might come about as a natural subproduct of the generation of vorticity explained in this paper, if it took place at different rates on the different cross sections of the tube along the axis. This can be the case, for instance, if the originally horizontal tube develops an omega-loop shape in which a stretch of it rises while the rest remains at the original level. If the tube was originally untwisted (or only weakly twisted), the rising sections would tend to turn into vortex tube pairs which contain most of the original magnetic flux. Now, in contrast to the 2D case, this rotation produces a transverse field component in the flanks of the rising section of the loop. If enough  $B_t$  is built up, the rotation in the vortices could be braked. Yet, a simple calculation shows that for this mechanism to be at all effective, the footpoint separation,  $\lambda$ , of the omega loop has to be small, in fact smaller than one pressure scaleheight. More precisely, if we require that the tube develops a transverse component of the level required by the criterion (11) after rising a distance equivalent to a few of its own radii, we obtain

$$\frac{\lambda}{H_p} \lesssim \left( \frac{R}{H_p} \right)^{1/2}. \quad (28)$$

This is a very small footpoint separation: the ratio of the Lorentz force associated with the curvature of the field lines to the buoyancy force in such a tube is at least of order  $H_p/\lambda$ . Consequently, it is not easy to raise a loop that is narrow enough for a sufficient pitch angle to develop at all. This is an indication that the tubes possibly have to be formed with the necessary amount of twist before they start to rise.

An interesting possibility for generating magnetic tubes with a non-zero total twist has been discussed by Cattaneo, Chiueh, & Hughes 1990: they consider a Rayleigh-Taylor unstable slab of plasma with horizontal magnetic field such that the angle subtended by the field vector with a fixed horizontal axis monotonically changes with depth. Upon development of the instability, the layer yields magnetic tubes with non-zero degree of twist. In their experiment, the authors showed how the resulting tubes were more resistant to deformation through the surrounding flows than in the corresponding untwisted case (Cattaneo & Hughes 1988). A corresponding three-dimensional problem has been calculated by Matthews, Hughes & Proctor 1995. They show how an unstable layer with a parallel horizontal field produces magnetic tubes with non-zero vorticity. Through nonlinear interaction, these tubes arch as they rise in a vertical plane, thereby becoming twisted.

Another open question concerns the fate of a twisted tube as it rises across successive density scaleheights in the convection zone. The internal and external densities are essentially equal for most of the rise (except for the small relative difference of order up to  $1/\beta \ll 1$ ): the tube thus expands and its field intensity weakens by several orders of magnitude along the journey (see Moreno-Insertis 1986, 1992, 1997b). In fact, the beginning of this process can be seen by comparing the maximum field intensity of the three panels of Fig. 8. The rate of decrease associated with an off-axis expansion of the tube, though, is different for the longitudinal and transverse components of the field (Parker 1979, §9). A rough but simple argument based on the conservation of flux in 2D yields a rate of change of the twist following an approximate law  $\tan \Psi \propto R$ . If so, the tubes could reach the upper convection zone with very large degrees of twist, possibly such that they can become kink unstable. Yet, three-dimensional effects could render that simple law of little use. The stretching of the tube apex in the longitudinal direction, for instance, a phenomenon common in Parker-unstable rising loops, may reduce the level of twist there. Also, the conservation of the total helicity in the tube could put an upper limit to the number of turns of the field lines around the axis at any single place. However it is, large pitch angles should be a common appearance in rising tubes when they reach photospheric levels. The sheared field structures observed in emerging active regions (Lites et al. 1995, Leka et al. 1996) may be a conse-

quence of this (see also Tanaka 1991, Kurokawa 1989 and Rust & Kumar 1996).

### 8.3. Magnetic tubes, air bubbles and rigid cylinders: similarities and differences

Along this paper we have compared our results to the laboratory experiments of flow past rigid cylinders and air bubbles at  $Re \cong 200 - 300$ . In the following we summarize the similarities and differences found.

*Magnetic tubes and air bubbles.* Remarkable similarities are: (a) the general shape and structural features (skirt, central tail) (b) the *protection* of the interior of the rising object through surface tension. These similarities are all the more striking given the difference in buoyancy [density deficit  $|\Delta\rho/\rho| \ll 1$  for the tubes,  $O(1)$  for the bubbles] and in the physical source of the surface tension (capillary effects vs. jump in the tangential field component). As a result, defining the Weber number on the basis of the corresponding surface tension mechanism, one can formulate a common law of dependence of structural properties on  $We$ .

*Magnetic tubes and rigid cylinders.* A clear similarity concerns the boundary layer: both objects have a no-slip condition along the boundary. Consequently, the relative jump of the tangential velocity across the boundary layer is large,  $[v_{tg}]/v_{tg} \sim O(1)$ . In contrast, there is a zero-tangential stress condition along the fluid/air interface of a bubble; correspondingly,  $[v_{tg}]/v_{tg} \sim O(Re^{-1/2})$ . As a result of the no-slip condition, both buoyant magnetic tubes and rigid cylinders produce (and shed downstream) secondary rolls near the point of separation of the boundary layer.

*Features specific to the buoyant magnetic tubes with twist.* In the magnetic tubes of the present simulations, the wake is formed in the initial phases of the rise out of material bodily transported from the initial tube. Thus, the wake is magnetized and maintains a magnetic connection to the head of the rising tube along time. The kind of behavior followed by the magnetic rope depends directly on the amount of magnetic flux incorporated into the wake, which, in turn, depends on the initial twist. In the case of an initially highly twisted tube ( $\Psi_{mt} = 13.9^\circ$ ), the magnetic rope is almost rigid and its shape and the flow around it strongly remind those of a *solid cylinder*. If the initial pitch angle is closer to the threshold (11), then the tube deforms and adopt a *bubble-like* shape (though it still satisfies a no-slip condition along its

boundary). Finally, if  $\Psi_{mt}$  is very small, the tube behaves like a rising *thermal* (Longcope et al. 1996).

This work was partially funded through the DGES project no. 95-0028-C of the Spanish Ministry of Education and Culture. The numerical calculations were carried out using the computing resources of the Instituto de Astrofísica de Canarias and of the Centre de Computació i Comunicacions de Catalunya. The authors are grateful to M. Kaisig for providing the numerical code and for his subsequent help with it. Thanks are also due to a large number of scientists in HAO, JILA and CORA in Boulder (Colorado) as well as in the University of Chicago for interesting discussions on the topic of this paper.

## REFERENCES

Batchelor, G.K., 1967, An Introduction to Fluid Dynamics, (Cambridge: CUP)

Bouard, R., Coutanceau, M., 1980, *J. Fluid Mech.*, 101, 583

Caligari, P., Moreno-Insertis, F., Schüssler, M., 1995, *ApJ*, 441, 886

Cargill, P.J., Chen, J., Spicer, D.S., Zalesak, S.T., 1996, *J. Geophys. Res.*, 101, 4855

Cattaneo, F., Hughes, D.W., 1988, *J. Fluid Mech.*, 196, 323

Cattaneo, F., Chiueh, T., Hughes, D.W., 1990, *J. Fluid Mech.*, 219, 1

Collins, R., 1965, *Chem. Eng. Sci.*, 20, 851

Collins, W.M., Dennis, S.C.R., 1973a, *Quart. J. Mech. Appl. Math.*, 26, 53

Collins, W.M., Dennis, S.C.R., 1973b, *J. Fluid Mech.*, 60, 105

Choudhuri, A.R., 1989, *Sol. Phys.*, 123, 217

Christov, C.I., Volkov, P.K., 1985, *J. Fluid Mech.*, 158, 341

Dandy, D.S., Leal, L.G., 1989, *J. Fluid Mech.*, 208, 161

Davies, R.M., Taylor, G.I., *Proc. R. Soc. Lond.*, A 200, 375

D'Silva, S., Choudhuri, A.R., 1993, *A&A*, 272, 621

Emonet, T., Moreno-Insertis, F., 1996, *ApJ*, 458, 783

Fan, Y., Fisher, G.H., DeLuca E.E., 1993, *ApJ*, 405, 390.

Fan, Y., Fisher, G.H., McClymont, A.N., 1994, *ApJ*, 436, 907

Fan, Y., Zweibel, E.G., Lantz, S.R., 1997, *ApJ*, submitted.

Hnat, J.G., Buckmaster, J.D., 1976, *Phys. Fluids*, Vol. 19, No. 2, 182

Hughes, D.W., Falle, S.A.E.G., Joarder, P., 1998, *MNRAS*, submitted.

Kaisig, M., Tajima, T., Shibata, K., Nozawa, S., Matsumoto, R., 1990, *ApJ*, 358, 698

Kurokawa, H., 1989, *Spa. Sci. Rev.*, 51, 49

Leka, K.D., Canfield, R.C., McClymont, A.N., van Driel-Gesztelyi, L., 1996, *ApJ*, 462, 547

Lites, B.W., Low, B.C., Martínez Pillet, V., Seagraves, P., Skumanich, A., 1995, *ApJ*, 446, 877.

Longcope, D.W., Fisher, G.H., Arendt, S., 1996, *ApJ*, 464, 999

Matthews, P.C., Hughes, D.W., Proctor, M.R.E., 1995, *ApJ*, 448, 938

Moreno-Insertis, F., 1983, *A&A*, 122, 241

Moreno-Insertis, F., 1986, *A&A*, 166, 291

Moreno-Insertis, F., 1992, in *Sunspots, Theory and Observations*, eds. J.H.Thomas and N.O.Weiss, p. 385 (Dordrecht: Kluwer).

Moreno-Insertis, F., 1997a, in *The inconstant Sun*, C. Marmolino and G. Cauzzi, eds., *Mem. Soc. Astr. It.* **68**.

Moreno-Insertis, F., 1997b, in *Solar Magnetic Fields*, Viggo Hansteen, ed., University of Oslo, p. 3–30.

Moreno-Insertis, F., Emonet, T. 1996, *ApJ*, 472, L53

Nordlund, Å, Stein, R.F. 1990, *Comput. Phys. Commun.*, 59, 119

Parlange, J.-Y., 1969, *J. Fluid Mech.*, 37, 257

Parker, E.N., 1979, *Cosmical Magnetic Fields*, (Oxford: Oxford University Press), chap. 9

Richtmyer, R.O., Morton, K.W. 1967, *Difference Methods for Initial-Value Problems* (2d ed.; New York: Interscience), chap. 13

Ryskin, G., Leal, L.G., 1984a, *J. Fluid Mech.*, 148, 1

Ryskin, G., Leal, L.G., 1984b, *J. Fluid Mech.*, 148, 19

Rubin, E.L., Burstein, S.Z., 1967, *J. Comp. Phys.*, 2, 178

Rust, D.M., Kumar, A., 1996, *ApJ*, 464, L199

Schüssler, M., 1979, *A&A*, 71, 79

Shibata, K. 1983, *PASJ*, 35, 263

Shibata, K., Tajima, T., Steinolfson, R.S., Matsumoto, R. 1989, *ApJ*, 345, 584

Stone, H.A., 1994, *Ann. Rev. Fluid Mech.*, 26, 65

Ta Phuoc Loc, 1980, *J. Fluid Mech.*, 100, 111

Ta Phuoc Loc, Bouard, R., 1985, *J. Fluid Mech.*, 160, 93

Tanaka, K., 1991, *Sol. Phys.*, 136, 37

Tsinganos, K.C., 1980, *ApJ*, 239, 746

Wegener, P.P., Parlange, J.-Y., 1973, *Annual Rev. Fluid Mech.*, 5, 79

This figure "figure1.jpg" is available in "jpg" format from:

<http://arXiv.org/ps/astro-ph/9711043v2>

This figure "figure2.jpg" is available in "jpg" format from:

<http://arXiv.org/ps/astro-ph/9711043v2>

This figure "figure5.jpg" is available in "jpg" format from:

<http://arXiv.org/ps/astro-ph/9711043v2>

This figure "figure7.jpg" is available in "jpg" format from:

<http://arXiv.org/ps/astro-ph/9711043v2>

This figure "figure9.jpg" is available in "jpg" format from:

<http://arXiv.org/ps/astro-ph/9711043v2>

This figure "figure13.jpg" is available in "jpg" format from:

<http://arXiv.org/ps/astro-ph/9711043v2>

This figure "figure14.jpg" is available in "jpg" format from:

<http://arXiv.org/ps/astro-ph/9711043v2>

This figure "figure16.jpg" is available in "jpg" format from:

<http://arXiv.org/ps/astro-ph/9711043v2>